

A Search for Planets Transiting the M Dwarf Debris Disk Host, AU Microscopii

Leslie Hebb^{1,2*}, Larry Petro³, Holland C. Ford², David R. Ardila^{2,5}, Ignacio Toledo⁶, Dante Minniti⁶, David A. Golimowski², Mark Clampin⁴

¹*School of Physics and Astronomy, University of St Andrews, North Haugh, St Andrews KY16 9SS, UK*

²*Department of Physics and Astronomy, The Johns Hopkins University, 3400 North Charles St, Baltimore MD 21218*

³*Space Telescope Science Institute, 3700 San Martin Drive, Baltimore MD 21218*

⁴*Spitzer Science Center, California Institute of Technology, Pasadena, CA 91125*

⁵*Department of Astronomy, Pontificia Universidad Católica de Chile, Casilla 306, Santiago 22, Chile*

⁶*NASA Goddard Space Flight Center, Code 681, Greenbelt, MD 20771.*

28 November 2021

ABSTRACT

We present high cadence, high precision multi-band photometry of the young, M1Ve, debris disk star, AU Microscopii. The data were obtained in three continuum filters spanning a wavelength range from 4500Å to 6600Å, plus H α , over 28 nights in 2005. The lightcurves show intrinsic stellar variability due to starspots with an amplitude in the blue band of 0.051 magnitudes and a period of 4.847 days. In addition, three large flares were detected in the data which all occur near the minimum brightness of the star. We remove the intrinsic stellar variability and combine the lightcurves of all the filters in order to search for transits by possible planetary companions orbiting in the plane of the nearly edge-on debris disk. The combined final lightcurve has a sampling of 0.35 minutes and a standard deviation of 6.8 millimag (mmag). We performed Monte Carlo simulations by adding fake transits to the observed lightcurve and find with 95% significance that there are no Jupiter mass planets orbiting in the plane of the debris disk on circular orbits with periods, $P \leq 5$ days. In addition, there are no young Neptune-like planets (with radii $2.5\times$ smaller than the young Jupiter) on circular orbits with periods, $P \leq 3$ days.

Key words: stars:individual:AU Mic – stars:late-type – circumstellar matter – stars:pre-main-sequence – planetary systems

1 INTRODUCTION

Observing planets around other stars and in various phases of their evolution is essential to understanding global properties of planetary systems and necessary for placing our own solar system in the context of planet formation theory. The detection of a young planet of known age in which the mass and radius can be measured (i.e. a transiting planet) would provide an unprecedented empirical test of extra-solar planet models and give information on the timescale of planetary formation. Further, the detection of a planet orbiting a debris disk star would allow investigation of the link between the planet forming disk and the planet itself. We have initiated a project designed to address these questions by searching for transiting planets around AU Microscopii (AU Mic, GJ 803).

AU Mic is a young ($\sim 8 - 20$ Myr,

Barrado y Navascues et al. (1999)), nearby (9.94 ± 0.13 pc, Perryman et al. (1997)) active M-dwarf (M1Ve) star in the β Pictoris moving group which is surrounded by a nearly edge-on circumstellar debris disk (Kalas et al. 2004; Krist et al. 2005). Observations of substructure in the disk suggest the presence of planetary-mass bodies. Such a companion which is close to the star and orbiting in the plane of the disk would transit, causing a dip in brightness. Thus, AU Mic is an excellent target to search for transiting planets in the early stages of formation.

Our photometric monitoring campaign that is designed to detect the signature of a transiting companion orbiting AU Mic is presented in this paper. The motivation for the project is discussed in § 2, In § 3, the observing program, the data processing, and the determination of differential photometry are explained. The results of the transit search and the parameter space in which we are sensitive to planets are described in § 4. In § 5, we briefly discuss the intrinsic

* E-mail: leslie.hebb@st-andrews.ac.uk

variability of the star, and conclusions and future work can be found in § 6.

2 AU MIC AND THE DEBRIS DISK

Direct observations of debris disks show small scale structure, including clumps and rings of dust and gaps clear of dust (e.g. Weinberger et al. 2003; Greaves et al. 2005; Clampin et al. 2003; Holland et al. 2003). Orbiting planets could give rise to such substructure as planets sweep up material and gravitationally influence the dust. A large planet would produce inner gaps cleared of dust, warp asymmetries and clumps of dust at mean motion resonances (Wyatt & Dent 2002; Wyatt et al. 1999; Quillen & Thorndike 2002) that are observed in debris disks.

IRAS first detected an excess of $60\mu\text{m}$ flux above purely photospheric emission around AU Mic, which was interpreted as circumstellar dust. Liu et al. (2004) and Chen et al. (2005) used broadband measurements between $25\mu\text{m}$ and $850\mu\text{m}$ to confirm the thermal emission from dust around the star. A single temperature modified black-body with temperature $T = 40 \pm 2\text{K}$ and spectral index $\beta = 0.8$ (Liu et al. 2004) provides a good fit to the observations. In addition, recent UV measurements of molecular hydrogen absorption lines place stringent constraints on the gas-dust ratio of less than 6:1 (Roberge et al. 2005), indicating the disk is gas poor. Thus, at an age of $\sim 8\text{-}20$ Myr most of the gas has been accreted onto the star or been removed from the system, and the star no longer contains a primordial, gas-rich star/planet-forming disk.

2.1 AU Mic Disk Structure

The proximity of AU Mic has allowed the debris disk to be imaged in scattered light in both optical and IR bands, within $\sim 10 - 210$ AU from the star, and at resolutions as high as 0.4 AU (Kalas et al. 2004; Krist et al. 2005; Liu 2004; Metchev et al. 2005; Masciadri et al. 2005). Very similar spatial features are observed independently in all the datasets, suggesting the debris disk is inclined nearly edge-on, is cleared of dust in the inner regions, and contains smallscale asymmetric clumps and gaps of material.

HST+ACS images show an edge-on disk with an inclination of $< 1^\circ$ from the line-of-sight within 50 AU of the star (Krist et al. 2005). Liu (2004) obtained images with Keck AO which resolved small scale structures in the disk in the region from 15-80 AU. These authors find asymmetries in the disk that cannot be explained by dust scattering properties and thus are assumed to be structural. The disk midplanes are unequal in length and radially confined bright and dark regions exist in both halves of the disk.

The cool dust temperature obtained through fitting the broad band SED (Liu et al. 2004) indicates a lack of warm dust in the inner disk near the star. According to this simple model, the 40K dust temperature translates into an evacuated area within 17 AU of the star. However, subsequent radiative transfer modelling of the scattered light finds smaller values of the disk inner radius. An evacuated area within 12 AU from the star is derived by Krist et al. (2005) through modelling of the optical scattered light. Metchev et al. (2005) combine their high resolution H-band

AO data with the existing optical data and broadband flux measurements to model the radiative transfer through the dust. The authors find the inner radius of the disk to be ≤ 10 AU. Due to the bright star, the inner edge of the disk is not directly observed in any current dataset.

As observations of the debris disk surrounding AU Mic suggest the presence of large bodies, several groups have recently attempted direct detections of thermal emission from large planets at distances of 10-60 AU from AU Mic using AO imaging (Metchev et al. 2005; Masciadri et al. 2005). However, no > 1 Jupiter mass (M_J) planets were detected at distances > 20 AU from the star and no $5 M_J$ planets were observed beyond 10 AU.

2.2 Possible Transiting Planets

Our group has taken a complementary approach to the search for planets around AU Mic by targeting the region < 0.25 AU from the star which is inaccessible with AO technology. Due to the edge-on aspect of the debris disk, close-in planets orbiting in the plane of the disk will transit the star. Adopting a 1° inclination for the disk and assuming a potential planet would orbit in the plane of the disk, we estimate the maximum period and separation at which orbiting planets will undergo transits.

Figure 1 shows the maximum transit depth as a function of planet mass and orbital period. We take the radius for AU Mic, $R=0.85 R_\odot$, from the stellar evolution models of Baraffe et al. (1998) for a 12 Myr, $0.5 M_\odot$ star and the planet properties from Baraffe et al. (2002) for the same age. We use the analytic transit model of Mandel & Agol (2002), which includes limb darkening, to derive the maximum transit depth. The theoretical planet radii do not vary much for planets ranging from $0.5 - 12 M_J$, thus according to our simple estimates, such planets on circular orbits with periods as large as ~ 70 days (orbital radius of $55 R_\odot$) will transit the star. Planets on ~ 40 day orbits will under go full, rather than grazing, transits causing dips in the lightcurve of > 30 mmag.

3 OBSERVATIONS

3.1 Observing Program

We monitored AU Mic between July 17 and August 14, 2005 with the CTIO-1m telescope and Y4K-Cam camera. The detector consists of a $4\text{K} \times 4\text{K}$ array of 15μ pixels placed at Cassegrain focus giving a $0.3''/\text{pixel}$ platescale. Thus the entire array projects to a $20' \times 20'$ FOV. The observed signal is fed into four amplifiers causing the raw images to have a quadrant effect with the readnoise between 11-12 e^- and gain of 1.45-1.52 e^-/ADU , depending on the amplifier. The detector has a readout time of 51 seconds and a 71k-electron well depth before non-linearity sets in. This converts to a saturation of 40,000 counts/pixel in 1×1 binning mode. However, with 2×2 binning, the readout time is reduced to 16 seconds, and the peak binned pixel value is limited by digital saturation to 65,535 counts.

AU Mic and the surrounding field were observed in four optical filters of medium width. These include a custom filter ($4520/200\text{\AA}$), Stromgren-y ($5497/241\text{\AA}$), and H α -off

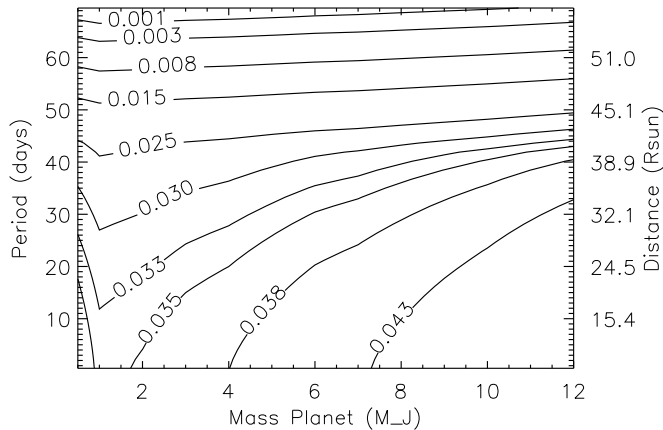


Figure 1. Contour plot of the maximum transit depth (mag) as a function of planet mass and orbital period for potential planets orbiting AU Mic. We assume the orbital plane of the planet is inclined 1° with the debris disk and adopt properties for AU Mic for a 12 Myr, $0.5 M_\odot$ star from Baraffe et al. (1998) and planet properties with masses from $0.5 - 12 M_J$ from Baraffe et al. (2002).

(6600/75Å) for continuum monitoring and $H\alpha$ (6563/75Å) for activity monitoring. The Stromgren-y, $H\alpha$, and $H\alpha$ -off filters, were available at the CTIO-1m for use with the Y4K-Cam. An image quality 3-cavity custom filter with central wavelength $\lambda_c=4520\text{\AA}$ and width= 200\AA was ordered from Custom Scientific. The filter is $4 \times 4 \times 0.3$ inches and is coated with anti-reflection material.

The narrow continuum filters allow us to isolate specific regions of the continuum free of highly variable chromospheric emission lines for optimal transit detection. The filters avoid the Hydrogen Balmer lines and the Ca II H & K lines associated with chromospheric emission, as well as the strong He features at 4026Å, 4686Å, and 5875Å, and the Na I doublet (5890Å and 5896Å) where emission peaks have been observed in absorption line cores of active M-dwarfs. In practice, the wavelength region covered by the Stromgren-y filter is shared by neutral metal lines (e.g. Fe I, Mg I, Ti I), and active M-dwarf stars are known to show very faint emission in these features during flares (e.g. Fuhrmeister et al. (2005); Paulson et al. (2006)).

The filters provide a wide spectral coverage to aid in distinguishing non-gray starspot variability from gray transits. In addition, the narrow filters allow us to take longer exposures that do not saturate the bright target star and that are less sensitive to instrumental systematics. Finally, we monitored in $H\alpha$ to identify residual variability in our continuum lightcurves caused by chromospheric activity.

Throughout each observing night, we monitored in all four filters alternating between $H\alpha$ and one of the continuum filters, systematically cycling through the continuum filters. We adopted 2×2 binning to obtain a faster readout time on the detector (hereafter, *pixel* refers to the binned 2×2 CCD pixel). Our observing program was designed to place the target on exactly the same detector pixels in order to minimize inaccuracies due to flat-fielding. In reality, the position of AU Mic varied within ~ 5 pixels from the chosen position. Exposure times were chosen to maximize the flux

in the target star and nearby reference stars while keeping the peak pixel value in AU Mic below $\sim 60,000$ counts. We defocused the telescope to avoid saturating AU Mic while taking longer exposures to build up signal in the fainter reference stars. We monitored during non-photometric weather and changed the exposure time continuously based on the photometric transparency. Thus, exposure times were varied between 3 – 40 seconds in all bands. In this way, a median sampling rate of 0.8 minutes was obtained for $H\alpha$ and ~ 2.5 minutes for all of the continuum filters. We observed AU Mic for 6-10 hours per night on 19 nights during that time. Due to poor weather, we obtained only 1-2 hours of data on 5 nights and completely lost an additional 5 nights.

3.2 Processing the Images

Flat field and bias calibration frames necessary for processing the images were obtained during each observing night. We took 2-D bias frames approximately every few hours in addition to sets of biases at the beginning and end of each night. At least 10 dome flats were observed per night in all four filters, and twilight flats (3-4 per filter) were obtained when the weather was clear.

The images were processed in a standard way using routines written by L. Hebb in the IDL programming language. Before performing any processing tasks, we checked for bad frames. Images in which the peak pixel value in AU Mic is equal to 65536 are saturated and those where the peak pixel value is less than 2000 counts have too low transparency to obtain useful magnitude measurements of the reference stars. There were typically ~ 10 out of ~ 1200 such images on a full night of observing which were removed from our processing list.

Each of the four amplifiers was processed independently. All object and calibration frames were first overscan corrected (by subtracting a line-by-line median overscan value) and then trimmed. We created nightly stacked bias images by average combining all bias frames observed each night. However, we noticed a smallscale 'herringbone' pattern in the bias frames which varied over the course of an observing night. This has subsequently been observed by other groups (see <http://www.lowell.edu/users/massey/obins/bias.html>). The amplitude of the variability is at the level of ± 10 counts/pixel, and it persists in our data. This corresponds to a maximum of 0.1% of the typical AU Mic flux and 0.3% of the combined flux of all the reference stars. Therefore, it contributes to the noise in the resulting lightcurves at the milli-mag level.

The stacked bias frames were subtracted from all object and flat field images. Average combined nightly dome flats were created in each filter, and each night, the object frames and any twilight flats that were obtained were divided by the stacked dome flat. After applying the dome flat correction, there is still residual large scale flat-field structure in the images which is stable over the course of the observing run. We tested the application of an additional illumination correction creating a stacked dome-flat corrected twilight flat, and divided this image by the object images. We applied this correction to several nights of data, but it did not provide any improvement to the resulting differential photometry. This is likely because we chose reference stars within $5'$ of

the target star over only a part of the detector in which the dome flats were a good match to the flat-field structure. As it did not improve the photometry, we did not apply this illumination correction to the data.

There is no apparent fringing structure in any of our images which span the wavelength range from 4500-6600 Å, including the continuum bands and H α . Thus, we do not apply a fringe correction. In addition, the exposure times are short and the dark current is negligible. We do not apply a dark current correction as its application would only add noise to our lightcurves. We obtained approximately 3300 observations of AU Mic in each of the continuum filters and \sim 9800 observations in H α .

3.3 Generating Lightcurves

3.3.1 Photometry

After the instrumental signatures were removed, source detection and aperture photometry were performed on all science frames using the CASU catalogue extraction software (Irwin & Lewis 2001). The software has been compared with SExtractor (<http://www.ast.cam.ac.uk/~wfcam/docs/reports/simul/>) and found to be very similar in the completeness, astrometry and photometry tests. The source detection algorithm defines an object as a set of contiguous pixels above a defined detection threshold. The routine requires as input the detection limit in units of background σ and the minimum number of connected pixels above that threshold which define an object. We set a detection threshold of 3 σ and a minimum source size of 15 pixels, so that AU Mic, the brightest star in the field, is easily detected in all the images. Potential comparison stars up to \sim 7 magnitudes fainter are also detected.

Aperture photometry with circular apertures was performed on the detected objects in all frames. The aperture size affects the precision of the differential photometry, thus the optimum aperture radius was chosen through empirical testing of several different sizes. An aperture which is too small will be susceptible to centering errors and can be affected by the pixelization of the detector, whereas an aperture which is too large will begin to include noise associated with sky pixels without adding much additional signal. Our experience with aperture differential photometry suggests that for bright stars, apertures larger than the median seeing produce lightcurves with lower rms.

The median seeing of our observations is \sim 1.5'' which corresponds to \sim 2.6 pixels (\sim 1.5''). Circular apertures with radii of 2.8, 4, and 8 pixels were tested on a single night of data. The same general features are present in the lightcurves generated with all the tested apertures, including the intrinsic stellar variability, but the 4 pixel (2.4'') aperture produced the AU Mic lightcurve with the smallest scatter. Thus, we obtained instrumental magnitude measurements for all detected objects on all frames by summing the background subtracted flux contained in the 4 pixel aperture.

3.3.2 Differential Photometry

To derive a differential photometry lightcurve for AU Mic from the instrumental photometry, we first correct for atmospheric extinction using magnitude measurements obtained on photometric nights for nearby, bright comparison stars. In each filter, we apply a linear least squares fit to the instrumental magnitudes as a function of airmass. The derived first order extinction coefficients are as follows: 0.21 for the 4520/200 filter, 0.14 for the 5497/245 filter, and 0.083 for the 6600/75 and H α filters. We apply these extinction corrections to all instrumental magnitude measurements. We note that this linear extinction correction is not strictly necessary since it is applied to all stars equally, and thus is removed when the differential magnitude is calculated. However, we correct for this well understood source of flux attenuation to derive an instrumental lightcurve which is dominated by the fluctuating atmospheric transparency, especially as caused by thin cirrus and other clouds

Next, we remove points from the lightcurves which were obtained under very poor observing conditions ($>$ 1.0 mags below the magnitude obtained under photometric conditions). In addition, we remove a handful of measurements obtained with exposure times $<$ 3s which are adversely affected by the finite shutter opening time. Finally, we derive the differential photometry lightcurve for AU Mic using the measurements of 13 comparison stars within \sim 5' and up to \sim 5 magnitudes fainter (in the 4520/200 band) than AU Mic.

Then we create a *super* comparison star lightcurve by averaging the instrumental magnitude lightcurves for the 13 individual stars (after subtracting the median value from each star). Initially, the 13 reference stars are weighted equally. Differential photometry lightcurves are then obtained for the individual comparison star lightcurves by subtracting the *super* lightcurve. Each comparison star is then assigned a weight value equal to the inverse variance of its differential photometry lightcurve normalized so that the weights of all 13 stars sum to one. The *super* comparison star lightcurve is then re-created, this time combining the individual lightcurves using a weighted average. The new *super* comparison star lightcurve is then subtracted from the instrumental AU Mic lightcurve. The resulting differential photometry lightcurves for AU Mic are shown in Figure 2 for the four filters. Since AU Mic is significantly brighter than the nearby reference stars used to derive the differential photometry, the lightcurve precision is dominated by photon Poisson noise in the reference star magnitude measurements. We have defined an error for each point on the lightcurve by taking the weighted standard deviation of the 13 comparison star objects used to derive that point on the AU Mic lightcurve.

3.3.3 Removing Intrinsic Variability

Figure 2 shows the intrinsic stellar variability previously observed in AU Mic (Rodono et al. 1986). We observe flare activity and sinusoidal variability indicative of starspots on the stellar surface. Both sources of variability are linked to magnetic activity and are typical for a young, active M-dwarf star, like AU Mic. The intrinsic variability of AU Mic is discussed briefly in § 5. However, the variability must be

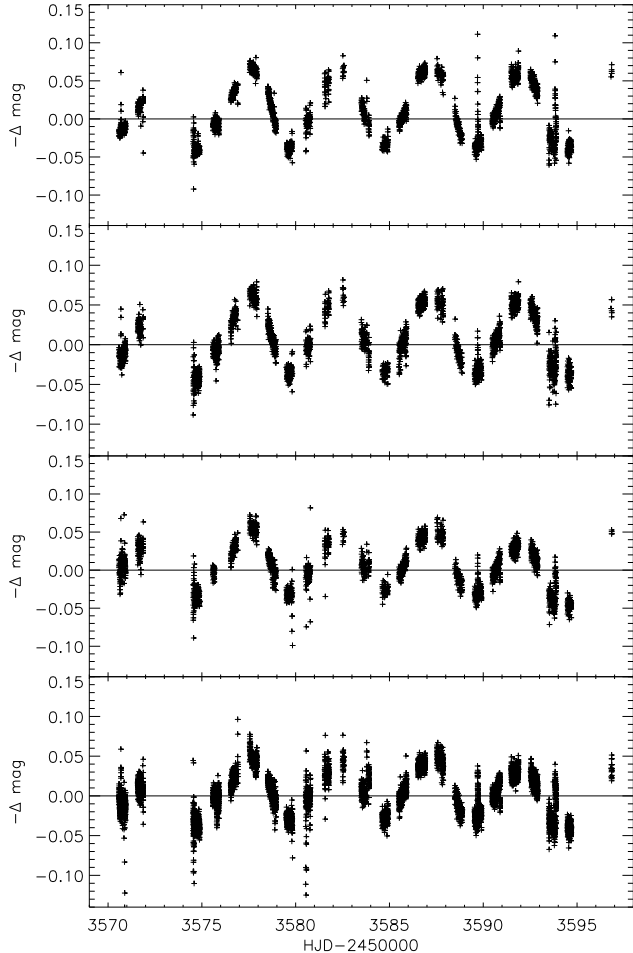


Figure 2. AU Mic differential photometry lightcurve in the four filters: F4520 (top), F5497 (middle-top), F6600 (middle-bottom), H α (bottom). Starspot variability and flaring are present in the data.

Table 1. HJD of Flare Cutout Regions

Flare	Beginning	End
Flare 1	2453570.68	2453570.73
Flare 2	2453589.69	2453589.77
Flare 3	2453593.82	2453593.90

removed in order to search for the signature of transiting planets in the lightcurve.

Both the shape and the timescale of these sources of variability differ significantly from that of a transit, so they do not induce contamination in the transit search. During our observing campaign, three large flares occurred on AU Mic which were detected in all four filters. During the flares, the magnitude of AU Mic increased sharply within minutes and then decayed slowly to its original value over an hour to a few hours. We simply remove the regions of the AU Mic lightcurves which include the three large flares. Table 1 gives the range of Heliocentric Julian Dates (HJDs) which are used to exclude points from the lightcurve near the time of the flares.

Table 2. Time Series Information

Filter	Number Points	Median Sampling (min)	Lightcurve RMS (mmag)	Correlated Noise (mmag)
F4520	3089	2.46	5.3	1.8
F5497	2960	2.46	7.3	1.8
F6600	2800	2.46	7.2	2.1
F6563	8737	0.70	7.6	2.3
Combined	17593	0.35	6.8	1.7

The quasi-sinusoidal, starspot variability occurs on timescales of ~ 5 days and varies in amplitude for the different filters. The Hipparcos period for this object is 4.8902 days, however we find the variation occurs on a 4.847 day timescale (see §5). To remove the modulation, we experimented with fitting a truncated fourier series to the phase-folded lightcurves in each filter as well as applying linear least-squares fits to the individual nights of data. We note that neither approach is a physical interpretation of the data or an attempt to model the starspots. Both techniques produce corrected lightcurves with similar noise properties, thus, for this analysis, we subtract a linear fit from each night of data to produce the AU Mic lightcurve for each filter which is removed of intrinsic variability. Table 2 gives the number of measurements in the corrected lightcurve for each filter, as well as the median sampling, the rms (weighted by the error bars) and the correlated noise on a 2-hour timescale, the typical planetary transit duration. To measure the correlated noise, we calculate the rms of the lightcurve where each point is replaced by the average of the points in a 2-hour window around that point (accounting for edge effects) (Pont et al. 2006). The rms of the smoothed lightcurve is 1.7 mmag which is higher than what is expected if the data were only white noise.

Since the transit signals for which we are searching will produce dips in brightness of the same depth in all four filters, we combine the four corrected lightcurves into a combined final AU Mic lightcurve, shown in Figure 3. The combined, intrinsic variability-corrected lightcurve is input into the periodic transit searching algorithm. The lightcurve contains 17593 points, has a median sampling of 0.35 minutes, and has an rms of 6.8 mmag (see Table 2).

4 SEARCH FOR TRANSITING PLANETS

4.1 Systematic Search for Periodic Transits: Applying the Box-Least-Squares Algorithm

The final, combined, intrinsic variability-corrected lightcurve was searched for features that could have been caused by a transiting planet. We performed a systematic search for periodic, square-shaped dips in brightness using the Box-Least-Squares algorithm of Kovács et al. (2002). We apply the algorithm to the final lightcurve, testing periods between 0.5 – 15 days. The short period limit is set by the Roche radius of a Jupiter mass planet around AU Mic, and the long period limit is approximately one half the duration of our monitoring campaign. Known short period, hot Jupiter planets have transit durations of a

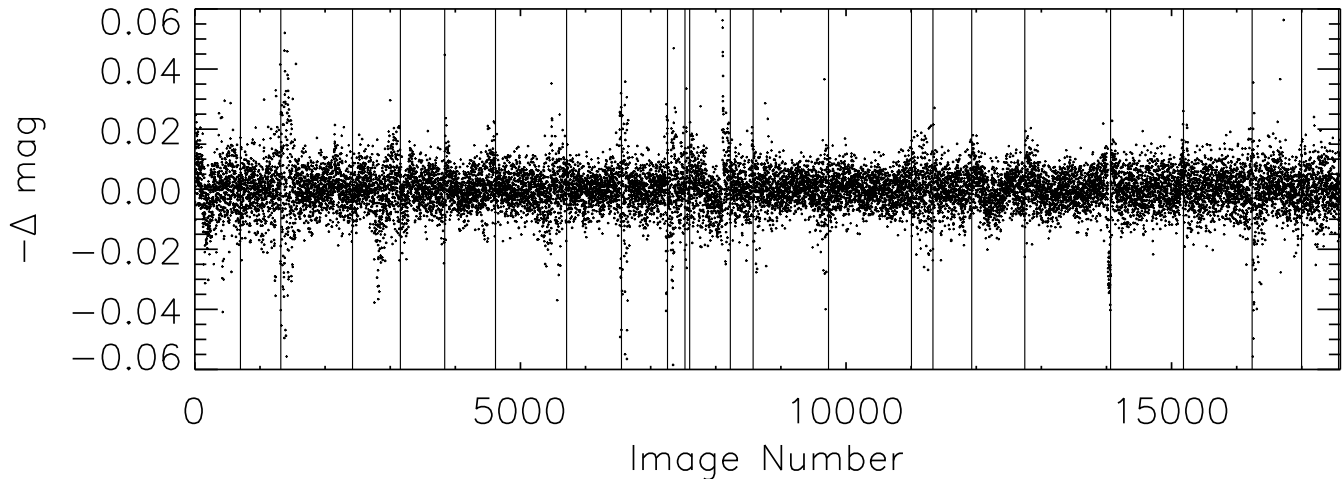


Figure 3. Combined, intrinsic variability-corrected, differential photometry lightcurve of AU Mic plotted versus image number. The data contain differential magnitudes for all four filters. They are removed of flares and corrected for the rotationally modulated starspot brightness. The vertical lines are placed at the positions of the night breaks.

few hours, thus we search for box-shaped dips with widths corresponding to planet durations from $\sim 1 - 5$ hours.

We employ a detection statistic, which identifies the signal-to-noise ratio, S/N, of the strongest dip in brightness as a function of trial period. The signal, S, is the depth of the candidate dip, and the noise, N, accounts for both random and correlated noise (Pont et al. 2006) as both contribute significantly to the noise in our final lightcurve. The S/N is given by:

$$S/N = \frac{\text{depth}}{\sqrt{\sigma^2/N_{intr} + \sigma_{red}^2/N_{tr}^2}}$$

where *depth* is the average depth of the transit-like event, σ is the average photometric error of the in-transit points, N_{intr} is the number of in-transit points, σ_{red} is the correlated noise on the typical transit timescale (2 hours) and N_{tr} is the number of detected transits. The resulting periodogram (S/N versus trial period) was then examined for significant peaks which would indicate periodic box-shaped dips in the lightcurve. We set a threshold of $S/N = 8.8$ to define a significant detection.

The detection threshold of $S/N = 8.8$ was derived from analysing a set of simulated lightcurves which contained only noise (no fake transits). We generated a set of 400 fake lightcurves with the same window function and noise properties of the observed lightcurve. This allows structure in the periodogram which arises due to the window function to mimic that of the observed lightcurve. The delta magnitude values are different for each simulated lightcurve and consist of the sum of a red noise component and a white noise component. The noise in each simulated lightcurve is randomly determined using the measured values given in Table 2.

The 400 simulated lightcurves, including only noise, were searched for transits in the same fashion as the observed data. We applied the box-fitting algorithm to each lightcurve and measured the peak S/N value that was detected. The algorithm typically finds a low level spurious

signal with a depth of ~ 2 mmag and a $S/N \sim 6$ in the simulated data. For the ensemble of simulated lightcurves, the distribution of output S/N values has a mean of 6.1 and a sigma of 0.9. 99.7% (3σ) of the simulated lightcurves produce a peak $S/N < 8.8$, so we adopt this value as the detection threshold to define significant periodic transits in the real data.

4.2 Detection and Analysis of Event: Is it Caused by a Transiting Planet?

The periodogram resulting from the periodic transit search on the intrinsic variability corrected AU Mic lightcurve is shown in Figure 4. There are many peaks in the periodogram above the significant detection level of $S/N=8.8$. From this, we infer that a significant box-shaped dip in brightness is present, however a unique period is not identified for it. Only one dip is apparent in a close visual inspection of the lightcurve, and the multiple peaks in the periodogram are likely due to the single event aliasing with the window function.

The single observed dip in brightness occurs in all four filters during the last 20 minutes of night JD 2453590. It consists of 39 data points, beginning at HJD= 2453590.884766 and continuing until the observing is stopped for the night at HJD= 2453590.898682. The average depth is 26.4 mmag, resulting in a $S/N = 10.0$. Figure 5 shows a blow-up of the lightcurve region which includes the transit-like event. The dip is clearly shown and is highly significant, however, it is not repeated, the ingress is very sudden, and the egress is not observed. Therefore, it is possible the dip is due to an instrumental, rather than astrophysical cause.

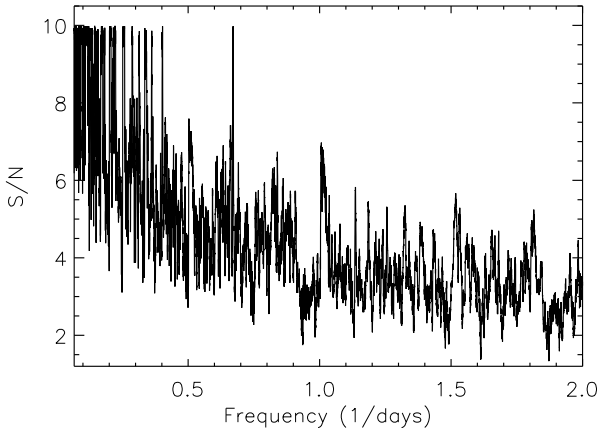


Figure 4. Periodogram resulting from the box-fitting algorithm.

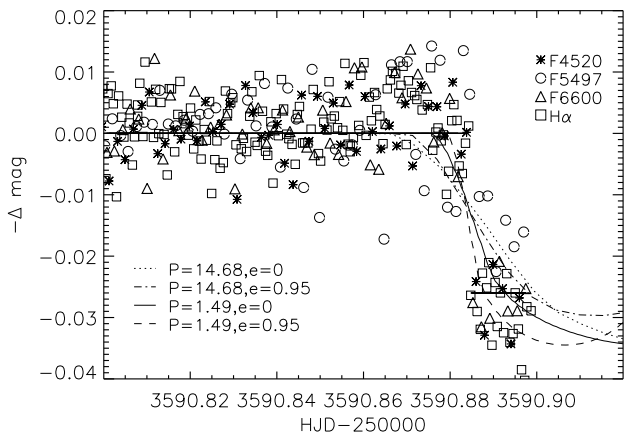


Figure 5. Lightcurve of AU Mic zoomed in on the detected dip in brightness. The data from the four filters are shown as different symbols (F4520, asterisks; F5497, circles; F6600, triangles; H α , squares). Four transit model lightcurves from Mandel & Agol (2002) are overplotted. The model lightcurves correspond to planets with orbital periods and eccentricities of: P=1.49 days, $e=0.0$ (solid), P=1.49 days, $e=0.95$ (dashed), P=14.48 days, $e=0.0$ (dotted), and P=14.48 days, $e=0.95$ (dot-dashed). We adopt a stellar radius of $R = 0.85 R_{\odot}$ (12 Myr, $0.5 M_{\odot}$ star (Baraffe et al. 1998) and a planet radius of $0.13 R_{\odot}$ to roughly reproduce the depth of the dip.

4.2.1 Considering Instrumental Explanations

We first examined the lightcurves of the individual reference stars for the night of JD 2453590. The reference stars showed no sudden brightness variations at the end of the night which would have caused the observed dip in the differential magnitude of AU Mic. We then checked for trends in the AU Mic lightcurve with instrumental properties. We plotted the data against the peak counts in AU Mic and its position on the detector, but found no correlation with the observed dip. On the same night, we checked for a relationship between the differential magnitudes and their corresponding airmasses, exposure times, background levels, and seeing measurements. Again, we found no correlation

between these instrumental properties and the differential photometry which could have caused the drop in brightness. In addition, we tested several photometric aperture sizes, and all showed the same dip in the lightcurve with the same depth and timing. Thus, we identified no systematic instrumental cause for the dip. However its nature is still uncertain. To determine whether the drop in brightness could have been caused by a transiting planet, we investigate the type of planet that would be required to be consistent with the observed lightcurve.

4.2.2 Depth and Period Constraints

If a transiting planet caused the observed dip in brightness, it would have to be quite large. The relationship between transit depth and planet radius can be approximated by $depth \sim 1.3 \times (R_p/R_s)^2$ (Tingley & Sackett 2005). Given a measured depth of 26.4 mmag and adopting a radius for AU Mic of $0.85 R_{\odot}$ (Baraffe et al. 1998), the planet radius is found to be $R_p \sim 1.1$ Jupiter radii. Although there are large uncertainties in the stellar evolution models used to define the stellar radius, and the depth equation is an approximation which is strictly only valid in the I-band, it is clear that only a planet with a Jupiter-like radius could account for the observed dip.

A transiting planet should show multiple dips in brightness occurring at periodic intervals. This was not observed. However, due to the window function of the lightcurve, it is possible that additional events occurred while we were not observing (e.g. during daytime or poor weather). Therefore, there are only certain periods between 0.5–15 days which are consistent with a transiting planet as the cause for the observed event. Peaks in the periodogram identify potential periods, which all have identical S/N values because they identify the same dip in brightness. The shortest possible transiting planet periods which are still consistent with the data are P=1.492 days, 2.484 days, and 3.870 days. The number of such periods increases with orbital period, with the longest one (within our search range) being P=14.680 days. Although, we are not sensitive to periodic signals longer than the duration of our observing campaign, we note that many possible planet periods outside our search range, between 15–70 days (see § 2.2), are also possible.

4.2.3 Constraints from the Ingress

The observed dip in brightness is very sharp with little or no apparent ingress. To determine whether a planet could cause such a sharp transit, we compared the observed dip to model lightcurves from Mandel & Agol (2002). Four model lightcurves which represent the extremes of the potential planets and which are consistent with the depth and period constraints defined above are overplotted on the data in Figure 5. Both the planet period and eccentricity affect the shape and duration of the ingress (if the depth of the transit and radius of the star are fixed), thus we try two different orbital periods of P=1.49 days and P=14.68 days, which both correspond to peaks in the periodogram. For both periods, we show the ingress curve of a planet with an eccentricity of $e = 0.0$ and $e = 0.95$ to represent the extremes at each period. We adopt a stellar radius, $R_s = 0.85 R_{\odot}$, for a

12 Myr, $0.5 M_{\odot}$ star (Baraffe et al. 1998) and a planet radius, $R_p = 0.13 R_{\odot}$, which is consistent with a Jupiter mass planet of this age and roughly reproduces the depth of the feature in the observed lightcurve. A quadratic limb darkening law is used with parameters found in Claret (2000) for a star with $T_{eff} = 3500$ K and $\log g = 4.0$.

The long period planet models ($P = 14.68$ days) shown here are inconsistent with the data due to their relatively long ingress compared to the sharpness of the observed dip. Consequently, planets on longer period orbits would also be unable to explain the data. The short period planet ($P = 1.49$ days) on a circular orbit ($e = 0.0$) is also largely inconsistent with the observed sharpness of the dip. The ingress of the short period planet on the highly eccentric orbit provides the closest match to the shape of the dip, however it still does not replicate the sharpness of the observed feature.

In summary, we placed constraints on the properties of a potential orbiting planet that could have caused the drop in brightness of AU Mic that was observed on JD 2453590. The combination of the deep, sharp, non-repeated dip makes it unlikely that the observed feature, shown in Figure 5, was caused by a transiting planet. In addition, there is no reason for us to believe the feature is caused by an instrumental problem. Therefore, we conclude this single event which mimicks a planetary transit is unexplained, and additional data is required to determine its true nature.

4.3 Search for Smaller Planets

In order to search for smaller planets in the data, we first remove the dip in brightness discussed in § 4.2 by subtracting the average depth of the dip (26.4 mmag) from the data points between HJD= 2453590.884766 and HJD= 2453590.898682. We then re-run the box-fitting algorithm. In this trial, the highest peak in the periodogram has a $S/N=6.4$, and thus is only consistent with noise. Therefore, we do not detect any significant, low-amplitude periodic box-shaped dips in brightness. The implications of this non-detection are discussed below.

4.4 Fake Transit Simulations

To set limits on the type of planet which could have been detected in our data, we generated simulated lightcurves with fake transits added to the observed data and tried to recover the transit signal.

In the simulations, we placed a planet in orbit around AU Mic in the plane of the debris disk (inclination angle equal to 1° from the line-of-sight). We adopted a host star radius of $0.85 R_{\odot}$ for a 12 Myr, $0.5 M_{\odot}$ star. The orbital phase of the simulated planet was chosen randomly from a uniform distribution, and the orbital period of the planet was chosen randomly from a uniform distribution within our search range (0.5–15 days). All simulated planets are assumed to be on circular orbits. We made no attempt to adopt the distribution of orbital properties of known planets since there are no observed data to constrain these values at the age of AU Mic. Noise-free model lightcurves were created using the analytic eclipse models of Mandel & Agol (2002) which were then added to a version of the observed

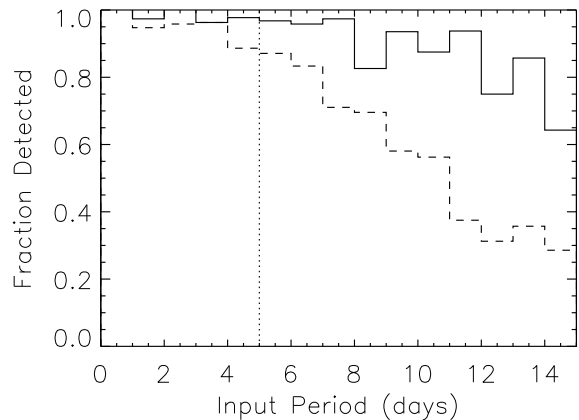


Figure 6. Fraction of simulated Jupiter-mass planets detected in the fake transit Monte Carlo simulations as a function of input orbital period. The solid line shows the fraction detected with a $S/N > 8.8$, and the dashed line shows the recovery fraction with a $S/N > 8.8$ and in which the period found by the box-fitting algorithm is within 5% of the input period (including twice and one-half aliases) (dashed line). The vertical dotted line corresponds to the 5 day period limit which is discussed in § 4.4.

data in which the detected dip in brightness described in § 4.2 was subtracted off. Thus, the simulated lightcurves with fake transits added have the same noise properties and sampling as the observed lightcurve.

The fake transit lightcurves were run through the box-fitting algorithm using the same search parameters as the observed data (searching for periods between 0.5–15 days and durations of ~ 1 –5 hours). The fake transits were considered recovered if the transit signature was detected with a $S/N \geq 8.8$ and the derived period was within 5% of the input orbital period. Alias periods which are one half or twice the input period are also considered recoveries.

We ran two sets of simulations (with 400 lightcurves each) using two different planet radii. First, we simulated a $1M_J$ planet in orbit around AU Mic adopting radius, $R_p=0.134 R_{\odot}$ for a 12 Myr, $1 M_J$ planet from Baraffe et al. (2002). Such a planet produces an unmistakable signal in the simulated lightcurves with a depth of > 30 mmag. The recovery fraction is a strong function of input period, as is shown in Figure 6 which plots the fraction of transiting Jupiter mass planets detected in the simulations as a function of input orbital period. If we consider only short period planets with periods, $P \leq 5$ days, 99% of the sample are significant detections with a $S/N > 8.8$ (solid line in Figure 6), and for 95%, the period is also correctly recovered (dashed line).

We ran an additional set of simulations using a planet which represents a possible Neptune-like planet at the age of AU Mic. Since the theoretical models do not reach the mass of Neptune and no young Neptune mass planets have been observed, we simply adopt a mass, $M = 0.05 M_{\odot}$, and a radius, $R = 0.054 R_{\odot}$, which is 2.5 times smaller than the radius of the 12 Myr old Jupiter. This type of planet produces a transit depth of ~ 5 mmag which is smaller than the noise limit of the data. However, for orbital periods, $P \leq 3$ days, 95% of the simulated transit lightcurves are detected with a

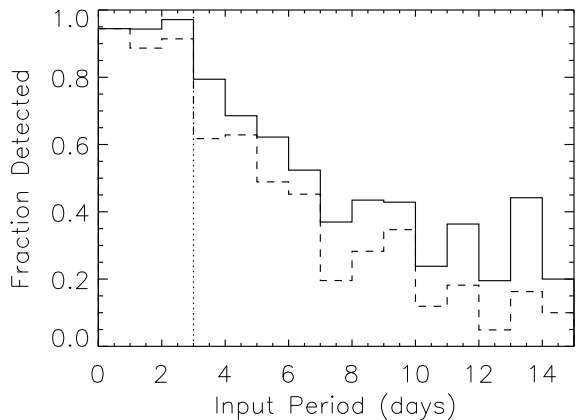


Figure 7. Results of the fake transit Monte Carlo simulations. Fraction of simulated Neptune-like planets, with a mass, $M=0.05 M_J$, and a radius, $R=0.054 R_\odot$, which is 2.5 times smaller than the radius of the 12 Myr old Jupiter. The solid line shows fraction detected with a $S/N > 8.8$, and the dashed line shows the recovery fraction with a $S/N > 8.8$ and in which the period found by the box-fitting algorithm is within 5% of the input period (including twice and one-half aliases) (dashed line). The vertical dotted line corresponds to the 3 day period limit which is discussed in § 4.4.

$S/N > 8.8$. In 92% of the cases, the period is also recovered. Figure 7 shows a plot of the fraction of transiting Neptune like planets detected in the simulations as a function of orbital period.

4.5 Interpretations

We interpret the results of the transit search on the observed lightcurve in the context of the fake transit simulations. Due to the lack of a convincing planetary transit detection in our observed lightcurve, we find, with 95% confidence, that there are no Jupiter mass planets on circular orbits around AU Mic with periods ≤ 5 days. We find at the 92% confidence level that there are no young planets with smaller radii (Neptune-like) orbiting AU Mic on circular orbits with periods ≤ 3 days.

It is important to note that the Monte Carlo simulations described above are based on theoretical stellar evolution models which are uncalibrated and untested by observations for low-mass stars and planets at the young age of AU Mic (Aigrain et al. 2007). In addition, early M-dwarfs are rapidly evolving in radius between 10-20 Myr, therefore, uncertainties in the age of AU Mic will produce uncertainties in the results of our simulations.

We combine our results with the constraints placed by adaptive optics imaging (Metchev et al. 2005; Masciadri et al. 2005) on the existence of planets orbiting in the outer parts of the AU Mic disk. In Figure 8, we show the region of parameter space as a function of planet mass and orbital separation in which an existing planet would have been detected. The existence of a planet in the hashed region of the diagram is ruled out with high significance due to the lack of a secure planet detection in either the adaptive optics or photometric monitoring

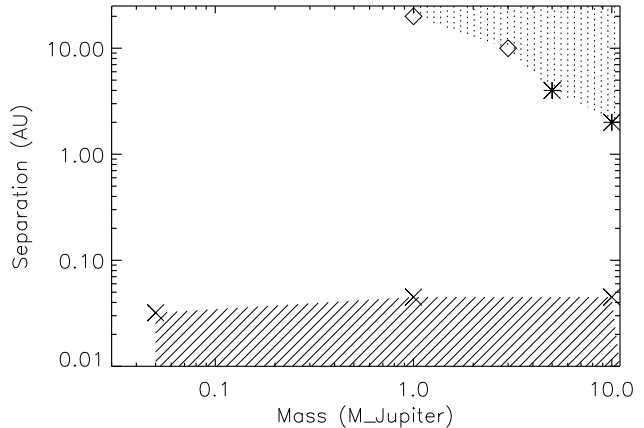


Figure 8. Region of planet parameter space as a function of planet mass and orbital separation showing the constraints on the existence of planets around AU Mic given by adaptive optics from Metchev et al. (2005, diamonds) and Masciadri et al. (2005, asterisks) and time series photometry (this work, crosses). The hashed areas show regions of the mass/separation parameter space in which the existence of a planet is ruled out with high significance.

dataset. There is still a large region of parameter space left to be explored. The search for transiting planets can potentially explore beyond the existing constraints out to 0.25 AU. Radial velocity measurements should be able to detect planets in the system out to several AU, however, the stellar activity will reduce the detection sensitivity of this method.

5 INTRINSIC STELLAR VARIABILITY

In addition to the planet search, the high cadence, multi-band photometric dataset described in this paper provides information about the intrinsic variability of AU Mic. We briefly report on the findings, but save a more in depth discussion, analysis, and modelling for a future paper.

5.1 Starspot variations

The stellar variability due to starspots is quasi-sinusoidal and periodic on the timescale of the stellar rotation period. We measure the periodicity in the lightcurve using a Lomb-Scargle periodogram (Scargle 1982) combining data from all the filters. The main peak in the periodogram is highly significant and occurs at 4.847 days. Our data covers approximately six rotations of the star, however with a period very close to 5 days, the phase coverage is incomplete. The period we derive is closer to the 4.854 day period found by Torres et al. (1972) than to the Hipparcos period of 4.8902 days.

The amplitude of the variability is a function of pass-band, indicating the wavelength dependence of the flux of the cool starspots causing the variability. Adopting our derived period, we perform a linear least squares fit of the phase-folded lightcurve with respect to a sine function to determine the amplitude of the initial fourier mode. The

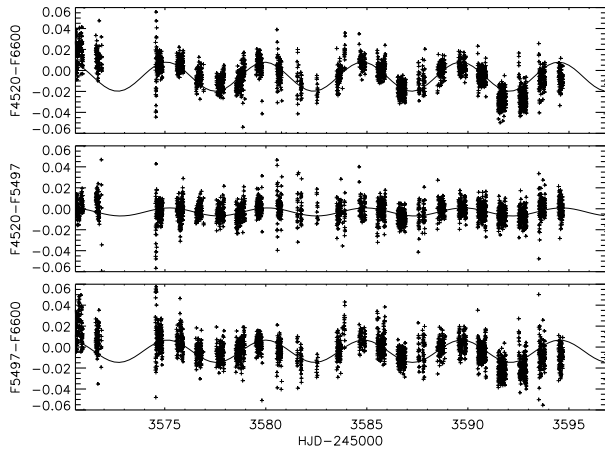


Figure 9. Lightcurves of the colors of the starspot variations. F4500-F6600 (top), F4500-F5497 (middle), and F5497-F6600 (bottom). Sine wave fits to the data are overlotted adopting the $P=4.847$ day period of the modulation.

amplitude of the variability is 0.051 mags, 0.047 mags, and 0.039 mags in the F4520, F5497, and F6600 filters. The $H\alpha$ band shows an 0.035 mag amplitude variability. The decrease in amplitude with wavelength is expected if the majority of starspots are cooler than the stellar photosphere. Figure 9 shows the colors of the variability emphasizing the change in amplitude of the modulation with wavelength.

5.2 Flare Activity

We report the detection of three large optical flares, observed in all four filters, during the month long monitoring campaign of AU Mic. Three of our filters show flaring of the continuum of the star; the $H\alpha$ filter represents the chromospheric activity. The observed flares show the characteristic structure of a rapid rise time and slower decay. They tend to occur when the star is near the minimum of the lightcurve which suggests they emanate from the most heavily spot covered hemisphere of the star. This has been observed in T Tauri flare stars such as V410 Tau (Fernández et al. 2004). Magnetic fields impede convection on the photosphere giving rise to starspots, thus it is not surprising that the flares, caused by magnetic activity, are associated with the heavily covered hemisphere of the star. A close-up of the lightcurve flare regions are shown in Figure 10.

We have measured the peak amplitude of the flares in each filter, as well as the rise time and exponential decay timescale. The values are found in Table 3. The continuum filters show increasing amplitude with decreasing wavelength. We resolve the rise time of the flare in $H\alpha$, but not in any of the other filters due to our higher $H\alpha$ sampling rate. However, the data suggest the faster the rise time of the flares, the faster the decay timescale. In addition, the shorter wavelength observations tend to show faster rise and decay timescales. Finally, there appears to be pre-flare absorption in the $H\alpha$ lightcurve which is most prominent before the first flare.

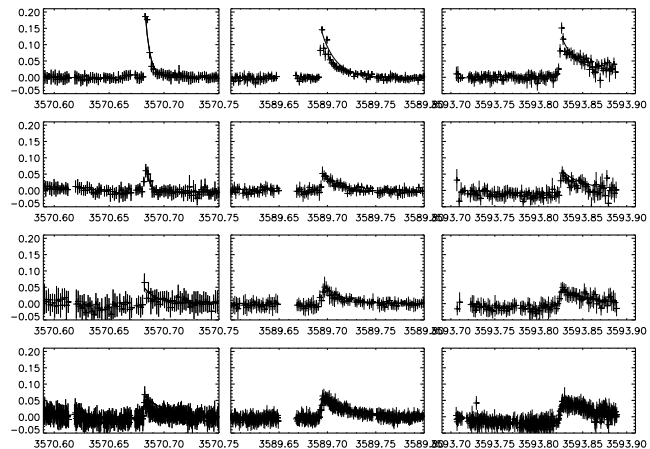


Figure 10. Regions of the lightcurves including the three flares observed flares. Flare 1 is shown in the left column F4500 (top), F5497 (second from top), F6600 (second from bottom), and $H\alpha$ (bottom) filters. Flare 2 is in the middle column, and Flare 3 is in the right column. The best fit exponential models to the decaying part of each flare are overlotted.

6 CONCLUSIONS AND FUTURE WORK

We have obtained unprecedented high cadence, high precision photometry of the young, M1Ve, debris disk star, AU Mic in four medium band filters over 28 nights. The combined lightcurve has a sampling rate of less than 1 minute and an rms (when the intrinsic stellar variability is removed) of 6.8 mmag. The lightcurve was searched for transiting extra-solar planets by applying a box-fitting algorithm designed to detect gray (same depth in all filters), periodic, square-shaped dips in brightness. We detected one significant event $S/N = 10.0$ which occurred at the end of the night in all four filters with a depth ~ 26.4 mmag. However, the constraints placed by the depth, period, and shape of the observed dip suggest it is unlikely to be caused by a transiting planet. More data is required to determine its nature. Therefore, in the observed lightcurve, we find no convincing transit events which could be caused by a planet orbiting AU Mic.

We performed Monte Carlo simulations by adding fake transits to the lightcurve to determine the probability of detecting a planet around AU Mic given the window function and noise properties of our data. The signature of a young Jupiter mass planet on a short period orbit would be easily detected. The results of the simulations indicate there are no planets with masses, $M > 1 M_J$ orbiting AU Mic in the plane of the debris disk ($\sim 1^\circ$) with periods, $P < 5$ days. A young Neptune-like planet with a smaller radius ($2.5\times$ smaller than the young Jupiter) could also be detected in our data. The lack of such a detection indicates there are no young Neptune-like planets orbiting AU Mic with periods, $P < 3$ days.

In addition to the transit search, the high cadence, multi-band photometry is ideal for examining the intrinsic stellar variability of the star due to starspots and flaring activity. AU Mic exhibits quasi-sinusoidal variability likely due to an uneven distribution of starspots on the stellar surface. The amplitude of the variability varies from 0.051 mags in the blue to 0.039 mags in the red. Using the periodic mod-

Table 3. Flare Properties

Flare	Filter	Start Time	Rise Time (min)	Exp Decay Timescale (min)	Peak Exp Fit (mag)	Peak Delta Mag (mag)
1	F4520	3570.68091	<2.8	6.2	0.195	0.183
1	F5497	3570.67993	2.5-4.9	5.3	0.076	0.063
1	F6600	3570.68042	<2.5	15.6	0.046	0.065
1	H α	3570.68140	0.7-1.4	26.5	0.064	0.070
2	F4520	3589.69092	2.5-4.9	21.3	0.138	0.147
2	F5497	3589.69165	2.1-4.6	20.4	0.054	0.053
2	F6600	3589.69043	7.0-9.5	27.6	0.052	0.053
2	H α	3589.69189	3.9-4.6	29.3	0.066	0.066
3	F4520	3593.81909	7.4-9.8	22.1	0.101	0.150
3	F5497	3593.82300	2.5-5.3	30.8	0.056	0.064
3	F6600	3593.82007	7.7-10.2	61.5	0.047	0.055
3	H α	3593.82275	4.2-5.3	33.5	0.052	0.052

ulation, we derive a stellar rotation period for the star of 4.847 days. We also report on the detection of three large optical flares which tend to emanate from the most heavily spotted hemisphere of the star. A more indepth analysis and modelling of the intrinsic stellar variability will be discussed in a subsequent paper.

New observations that were obtained in August and September of 2006 using the CTIO-1m and Australian National Universty (ANU) 40-inch telescope will help place further constraints on the existence of planets around AU Mic and allow improved modelling of the intrinsic stellar variability.

ACKNOWLEDGMENTS

DM and IT are partially supported by Fondap Center for Astrophysics 15010003. This research was supported in part by NASA grant NAG5-7697.

REFERENCES

Aigrain, S., Hodgkin, S., Irwin, J., Hebb, L., Irwin, M., Favata, F., Moraux, E., & Pont, F. 2007, MNRAS, 375, 29
 Barrado et al. 1999, ApJL, 520, L123
 Baraffe, I., Chabrier, G., Allard, F., & Hauschildt, P. H. 1998, A&A, 337, 403
 Baraffe, I., Chabrier, G., Allard, F., & Hauschildt, P. H. 2002, A&A, 382, 563
 Chen, C. H., et al. 2005, ApJ, 634, 1372
 Clampin, M., et al. 2003, AJ, 126, 385
 Claret, A. 2000, A&A, 363, 1081
 Fernández, M., et al. 2004, A&A, 427, 263
 Fuhrmeister, B., Schmitt, J. H. M. M., & Hauschildt, P. H. 2005, A&A, 439, 1137
 Greaves, J. S., et al. 2005, ApJL, 619, L187
 Haisch, K. E., Jr., Lada, E. A., & Lada, C. J. 2001, ApJL, 553, L153
 Holland, W. S., et al. 2003, ApJ, 582, 1141
 Irwin, M. & Lewis, J. 2001, NewAR, 45, 105
 Kalas et al. 2004, Science, 303, 1990

Kovács, G., Zucker, S., & Mazeh, T. 2002, A&A, 391, 369
 Krist, J. E., et al. 2005, AJ, 129, 1008
 Liu et al. 2004, ApJ, 608, 526
 Liu, M. 2004, Science 305, 1442
 Mandel, K., & Agol, E. 2002, ApJL, 580, L171
 Masciadri, E., Mundt, R., Henning, T., Alvarez, C., & Bar-rado y Navascués, D. 2005, ApJ, 625, 1004
 Metchev, S. A., Eisner, J. A., Hillenbrand, L. A., & Wolf, S. 2005, ApJ, 622, 451
 Paulson, D. B., Allred, J. C., Anderson, R. B., Hawley, S. L., Cochran, W. D., & Yelda, S. 2006, PASP, 118, 227
 Perryman, M. A. C., et al., 1997, The Hipparcos and Tycho Catalogues, ESA SP-1200.
 Pont, F., Zucker, S., & Queloz, D. 2006, MNRAS, 1146
 Quillen, A. C., & Thorndike, S. 2002, ApJL, 578, L149
 Roberge, A., Weinberger, A. J., Redfield, S., & Feldman, P. D. 2005, ApJL, 626, L105
 Rodono, M., et al. 1986, A&A, 165, 135
 Scargle, J. D. 1982, ApJ, 263, 835
 Strom, S. E., & Edwards, S. 1993, ASP Conf. Ser. 36: Planets Around Pulsars, 36, 235
 Tingley, B., & Sackett, P. D. 2005, ApJ, 627, 1011
 Torres, C. A. O., Mello, S. F., & Quast, G. R. 1972, ApJL, 11, 13
 Weinberger, A. J., Becklin, E. E., & Zuckerman, B. 2003, ApJL, 584, L33
 Wyatt, M. C., & Dent, W. R. F. 2002, MNRAS, 334, 589
 Wyatt, M. C., Dermott, S. F., Telesco, C. M., Fisher, R. S., Grogan, K., Holmes, E. K., & Piña, R. K. 1999, ApJ, 527, 918